

Parameters of Star Formation Regions in Galaxies NGC 3963 and NGC 7292

A. S. Gusev,¹ F. Kh. Sakhibov,² A. V. Moiseev,^{3,1} V. S. Kostiuk,¹ and D. V. Oparin³

¹ Sternberg Astronomical Institute, Moscow State University, Moscow, Russia

² University of Applied Sciences, Technische Hochschule Mittelhessen, Friedberg, Germany

³ Special Astrophysical Observatory, Russian Academy of Sciences, Nizhnii Arkhyz, 369167 Russia

Received March 6, 2024; revised May 2, 2024; accepted June 4, 2024

Abstract. Results of a study of physical parameters of stellar population in star formation regions in galaxies with signs of peculiarity NGC 3963 and NGC 7292 are presented. The study was carried out based on the analysis of photometric (*UBVRI* bands), $H\alpha$ and spectroscopic data obtained by the authors, using evolutionary models of stellar population. Among 157 star formation regions identified in galaxies, the young stellar population mass estimates were obtained for 16 of them and the age estimates were obtained for 15. The age of star formation regions clearly correlates with the presence of emission in the $H\alpha$ line: HII regions in the galaxies are younger than 6-8 Myr, and the regions without gas emission are older. The studied objects are included in the version 3 of our catalogue of photometric, physical and chemical parameters of star formation regions, which includes 1667 objects in 21 galaxies. Key aspects of the technique used to estimate the physical parameters and different relations between observational and physical parameters of the young stellar population in star formation regions are discussed.

Keywords: spiral galaxies, peculiar galaxies, star formation, HII regions, stellar population

DOI: 10.1134/S1063772924700616

1. INTRODUCTION

The processes of modern star formation, observed over a wide range of wavelengths (from ultraviolet to infrared) in most spiral and some lenticular galaxies, are among the most visible indicators of galaxy evolution in the present epoch. Stars form in groups within the densest and coldest parts of giant molecular hydrogen clouds. The largest groups of newborn stars, known as stellar complexes, can reach sizes of 600–700 pc (Efremov, 1989; Elmegreen, 1994; Efremov, 1995; Elmegreen & Efremov, 1996; Efremov & Elmegreen, 1998; Odekon, 2008; Elmegreen, 2009; de la Fuente Marcos & de la Fuente Marcos, 2009; Portegies Zwart et al., 2010). These complexes consist of smaller groupings such as OB associations, star clusters, and star aggregates (Efremov et al., 1987; Ivanov, 1991).

The main indicator of star formation in the optical range is the emission from HII regions in the Balmer hydrogen lines, primarily in the $H\alpha$ line. The ionization of hydrogen is caused by the most massive stars. However, star formation regions (SFRs) younger than 1–2 Myr are

not observed in optical wavelengths due to significant extinction by the dust cocoon surrounding the star-gas grouping (Whitmore et al., 2011; Hollyhead et al., 2015; Kim et al., 2021). The lifespan of an HII shell does not exceed 8-10 Myr.

Data on the physical and chemical parameters of stars and gas in SFRs, such as size, metallicity, mass, and age, are crucial for understanding modern evolutionary processes in disk galaxies. Particularly challenging in unresolved groupings are the correct accounting for extinction in SFRs, the separation of the contributions of stellar and gas emissions in broad photometric bands, and the accounting for the effect of discreteness of the initial mass function (IMF) for low-mass star clusters and associations (Piskunov et al., 2011; Cerviño, 2013; Gusev et al., 2016, 2018, 2023b). The research method used will be described in detail in Section 3.

In recent years, several large international projects such as LEGUS (Calzetti et al., 2015), PHANGS-MUSE (Emsellem et al., 2022), and PHANGS-*HST* (Lee et al., 2022) facilitated the study of tens of thousands of young star clusters, OB associations, and HII regions in many galaxies (Adamo et al., 2017; Whitmore et al., 2021;

Send offprint requests to: Alexander S. Gusev, e-mail: gusev@sai.msu.ru

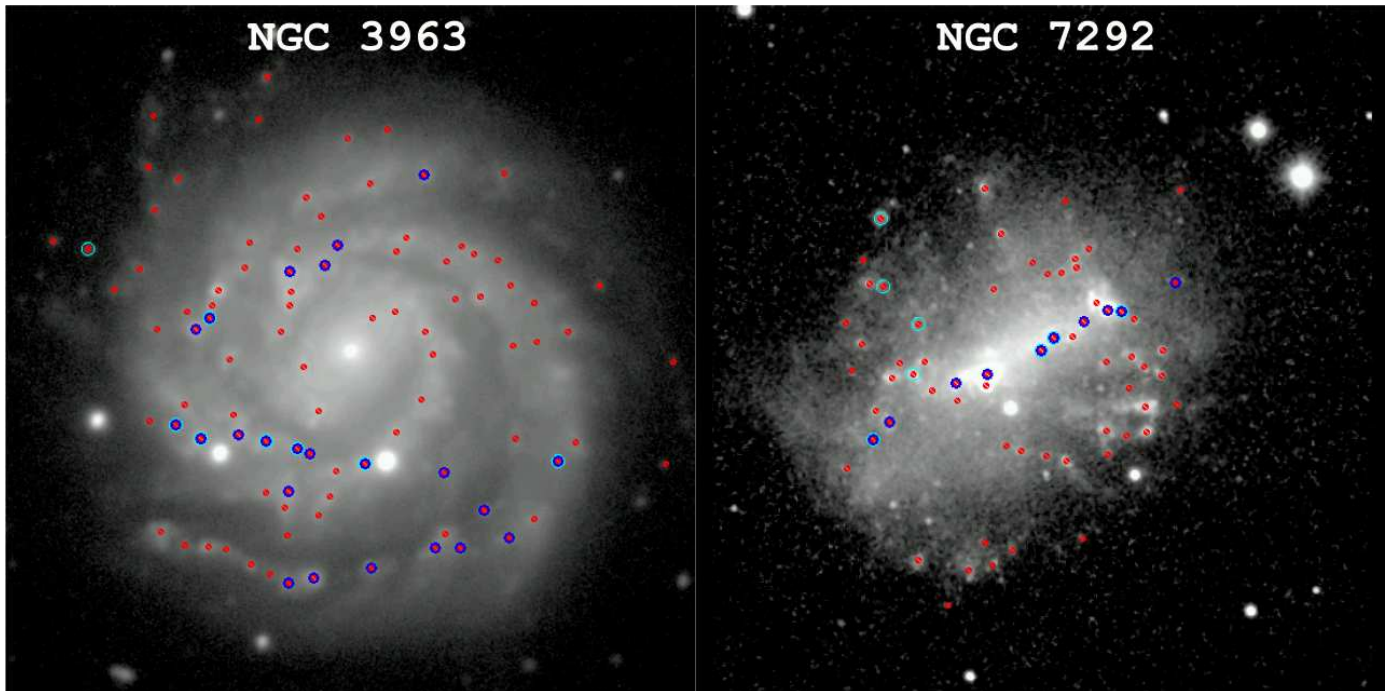


Fig. 1. Images of the galaxies NGC 3963 (left) and NGC 7292 (right) in the band on a logarithmic intensity scale. Red small circles indicate identified SFRs studied photometrically, blue circles denote SFRs studied spectroscopically in Gusev & Dodin (2021), and large cyan circles represent SFRs with obtained mass (age) estimates in this study. The image size for NGC 3963 is $170.5'' \times 170.5''$, corresponding to a linear size of 40.67 kpc, and the image size for NGC 7292 is $146.7'' \times 146.7''$ (4.85 kpc). North is up, east is to the left. The centers of the images correspond to the centers of the galaxies.

Thilker et al., 2022; Larson et al., 2023; Groves et al., 2023). Generally, HII regions and young stellar groupings are considered separately within these projects. In particular, the age and mass of young stellar groupings and extinction in the star formation region are determined by comparing the spectral energy distribution with theoretical evolutionary models (see, e.g., Turner et al., 2021) without using extinction data from HII regions obtained from spectroscopic observations. In recent years, several studies have jointly considered the properties of stellar populations and gas in HII regions. However, even in these studies, the age and mass of the stellar population are determined without extinction data from spectral observations. For example, in Scheuermann et al. (2023), the authors studied the properties of stellar populations in HII regions by comparing data from the PHANGS-MUSE and PHANGS-*HST* catalogs but did not use Balmer extinction data to estimate the ages of young stars. Unlike those studies, we investigate the properties of stellar populations in HII regions using both photometric and spectral data (see Section 3 for more details).

The main goal of the study is to estimate the physical parameters (mass and age) of the stellar population in SFRs based on comprehensive photometric, spectrophotometric, and spectroscopic observations of galaxies. Previously, in our series of works (see Gusev et al., 2023b, and references therein), we reviewed and analyzed a sample of 1510 SFRs in 19 galaxies based on photo-

metric data in the *UBVRI* and the $H\alpha$ line, as well as spectroscopic results of the associated HII regions. The catalog of studied regions is available in electronic form.¹ In this study, we extend our sample to SFRs in two more galaxies: NGC 3963 and NGC 7292.

Both galaxies studied by us using spectroscopy in Gusev & Dodin (2021) are interesting due to their various peculiarities. The SAB(rs)bc-type galaxy NGC 3963 has an almost perfectly symmetrical shape (Fig. 1). However, an excess of oxygen and nitrogen is observed in the HII regions in the outer part of the galaxy's southern spiral arm, possibly explained by the inflow of metal-enriched gas into the southwest part of NGC 3963 (Gusev & Dodin, 2021). The shape of the southern spiral arm deviates from a classic logarithmic spiral (Fig. 1), and HI observational data analysis results indicate tidal distortions in NGC 3963 and the galaxy NGC 3958, located 110 kpc southwest of it (van Moorsel, 1983). The Magellanic-type galaxy NGC 7292, with a bright asymmetric bar (Fig. 1), has rather complex kinematics: radial movements related to the bar play a significant role, and some non-circular motions at the southeast end of the bar – the brightest HII region – may be associated with the aftermath of a merger with a companion (Gusev et al., 2023a).

Basic information about the galaxies – coordinates of the center, morphological type, apparent magnitude

¹ http://lnfm1.sai.msu.ru/~gusev/sfr_cat.html

Table 1. Main characteristics of the galaxies

Parameter	NGC 3963	NGC 7292
Coordinates of the center: α, δ (J2000)	11 ^h 54 ^m 58.7 ^s +58°29′37.1″	22 ^h 28 ^m 25.3 ^s +30°17′35.3″
Type	SAB(rs)bc	IBm
$m(B)$, mag	12.60 ± 0.07	13.06 ± 0.06
$M(B)_0^i$, mag	−21.1 ± 0.3	−16.7 ± 1.0
i , degr	29	29
PA, degr	96	73
d , Mpc	49.2	6.82
D_{25} , arcmin	2.57	1.91
D_{25} , kpc	36.8	3.78
$A(B)_G$, mag	0.083	0.223
$A(B)_{in}$, mag	0.09	0.14

$m(B)$, corrected for galactic extinction and disk inclination extinction, absolute magnitude $M(B)_0^i$, inclination i and positional angle PA of the disk, distance d , diameter at the isophote 25^m in the B band considering galactic extinction and extinction caused by the disc inclination (D_{25}), galactic extinction $A(B)_G$, and extinction caused by the inclination of the galactic disk $A(B)_{in}$ – are provided in Table 1. The galaxy data were taken from the NED² and HyperLEDA³ open databases. Exceptions are the data for the center coordinates, inclination, and positional angle of the NGC 7292 galaxy, for which we used values from Gusev et al. (2023a).

2. OBSERVATIONS AND DATA REDUCTION

Spectral observations with a long slit conducted in 2020 on the 2.5-m telescope at the Caucasian Mountain Observatory (CMO) of the Sternberg Astronomical Institute of Moscow State University (SAI MSU) using the transient double-beam spectrograph (TDS) (Potanin et al., 2020), are detailed in Gusev & Dodin (2021). In total, data for 23 HII regions in NGC 3963 (including several objects previously observed within the SDSS project⁴) and 9 in NGC 7292 were obtained and analyzed.

Photometric observations of NGC 3963 in $UBVRI$ bands were conducted in 2020 on the 2.5-m telescope at the CMO SAI MSU at the Cassegrain focus $f/8$ (see the observation log in Table 2). The NBI CCD camera, equipped with two detectors of 2048×4102 px, provided an image field of $10.5' \times 10.5'$ at a scale of $0.155''/\text{px}$. Observations of NGC 7292 were conducted in 2005 on the 1.5-m telescope at Maidanak Observatory of the Astronomical Institute of the Academy of Sciences of Uzbekistan (Uzbekistan) using the SITE-2000 CCD camera at the 1:8 focus. The matrix size was 2000×800 px, providing a field of view of $8.9' \times 3.6'$ at a scale of $0.267''/\text{px}$ (Artamonov et al., 2010). Further processing followed the

Table 2. Observation log

Galaxy	Dates	Band	Exposure, s	ϵ^*		
NGC 3963	13/14.04.2020, 14/15.12.2020	U	3000	2.0″		
		B	1500	2.2		
	07/08.11.2021	V	750	2.1		
		R	450	1.9		
		I	300	1.8		
		$H\alpha$	2100	1.8		
		[NII]	1200	1.7		
		$H\alpha_{cont}$	1800	1.9		
		NGC 7292	25/26.10.2005	U	1200	1.4
				B	600	0.9
13/14.12.2020, 14/15.12.2020	V	480	1.0			
	R	360	1.0			
	I	240	0.8			
	$H\alpha + [NII]$	1050	0.9			
	$H\alpha_{cont}$	1200	0.9			

* ϵ is the image seeing.

standard procedure using the ESO-MIDAS image processing system (see, e.g. Bruevich et al., 2010). To construct color equations and account for atmospheric extinction, observations of standard stars from the Landolt fields PG 0231+051, PG 2331+055, J125239+444615, GD 279, and GD 300 (Landolt, 1992, 2013; Clem & Landolt, 2016) were used, obtained on the same nights in the corresponding filters. The color transformation equations from the instrumental photometric system to the standard Johnson–Cousins $UBVRI$ system are detailed in Artamonov et al. (2010) for the Maidanak Observatory telescope and in Gusev et al. (2018) for the CMO.

The galaxy NGC 3963 is quite distant from us (see Table 1), and its $H\alpha$ emission lies outside the narrow-band $H\alpha + [NII]$ filters available in the NBI camera set, centered at a wavelength of $\lambda = 6563\text{\AA}$, with a typical bandwidth $\Delta\lambda \sim 60 - 80\text{\AA}$. Therefore, its observations in the $H\alpha$ and $[NII]\lambda 6584$ lines were conducted in 2021 on the 2.5-m telescope at CMO in the Nasmyth focus using the MaNGaL narrow emission line mapper – a photometer with a tunable filter based on a low-order Fabry-Perot interferometer with an instrumental $FWHM = 13\text{\AA}$ (Moiseev et al., 2020). The detector of the instrument is the Andor iKon-M934 CCD camera with 1024×1024 px, providing images of $5.6' \times 5.6'$ at a scale of $0.33''/\text{px}$ on this telescope. During the observations, images were sequentially obtained at wavelengths corresponding to the $H\alpha$, $[NII]\lambda 6584$ emission lines and the continuum at $40 - 50\text{\AA}$ both sides from the $H\alpha$ line, considering the systemic velocity of the galaxy. The duration of individual exposures was 300 s, and only frames with the best image quality were used in the further analysis. The total exposure times are listed in Table 2. The observations were processed according to the algorithms described in Moiseev et al. (2020), and the absolute flux calibration was performed using images of the spectrophotometric standard AGK+81°266, obtained

² <http://ned.ipac.caltech.edu/>

³ <http://leda.univ-lyon1.fr/>

⁴ <http://skyserver.sdss.org/dr16>

on the same night just before the galaxy observations, at a similar air mass.

Observations in the $H\alpha+[NII]$ filter for the galaxy NGC 7292 were conducted in December 2020 on the 2.5-m telescope at CMO using the same NBI camera as in the photometric observations of NGC 3963. The standard narrowband $H\alpha+[NII]$ filter at the observatory has a peak transmission at $\lambda_{\text{cent}} = 6558\text{\AA}$ and a half-width $\Delta\lambda = 77\text{\AA}$. To measure the continuum, a filter with $\lambda_{\text{cent}} = 6427\text{\AA}$, $\Delta\lambda = 122\text{\AA}$ was used.⁵ For absolute calibration, a FITS image of the galaxy from James et al. (2004), taken from the NED database, was used.

3. METHODS OF RESEARCH

The research methods used in this study have been previously detailed in Gusev et al. (2016, 2018, 2023b). The algorithm includes identifying SFRs using the SExtractor software in the B and $H\alpha$ bands, determining the sizes of SFRs, their morphology, and their relationship with HII regions, photometry of SFRs in individually selected apertures in $UBVRIH\alpha$, accounting for the contribution of gas emission in the $UBVRI$ bands, accounting for extinction in SFRs using spectral data (specifically the Balmer decrement), and estimating the mass and age of the stellar population in SFRs by comparing the luminosities and color indices of SFRs with a grid of evolutionary models calculated based on stellar evolutionary tracks library (version 2.8),⁶ developed by the Padova group (Bertelli et al., 1994; Bressan et al., 2012; Tang et al., 2014). This grid corresponds to the metallicity on the color-luminosity and two-color diagrams, and the method involves finding the minimum of a deviation functional between observed values and the grid nodes. The deviation functional is defined as

$$\begin{aligned} & [((U - B)_{\text{obs}} - (U - B)_{\text{model}})^2 \\ & + ((B - V)_{\text{obs}} - (B - V)_{\text{model}})^2 \\ & + [M(B)_{\text{obs}} - M(B)_{\text{model}}]^2]^{1/2}, \end{aligned} \quad (1)$$

where the subscript "obs" denotes observed luminosities and color indices, and "model" denotes model luminosities and color indices.

The result of this method is the determination of the following parameters of the SFRs: their sizes, gas metallicity, mass, and age of the stellar population. A detailed description of the resulting electronic catalog of SFRs is presented in Gusev et al. (2023b). In this section, we focus on two key aspects of our methodology that posed the most significant challenges.

3.1. Accounting for Extinction in SFRs

The first key aspect concerns the correct accounting of extinction in the star formation region. Extinction is determined by the Balmer decrement of the gas emission in

HII regions. Using this value to account for extinction in the young stellar system in the $UBVRI$ bands is only possible if the stellar extinction equals the extinction in the gas cloud.

The evolutionary morphological sequence of SFRs (Whitmore et al., 2011) describes several stages of the development of a star-gas-dust region (see Whitmore et al., 2011, Fig. 1). For young clusters that are unresolved into individual stars in the optical range, four development stages can be identified:

- (1) emission in $H\alpha$ is observed, but no emission is seen in short-wavelength photometric bands;
- (2) emission from both gas (in the $H\alpha$ line), and stars (in broad photometric bands) is observed, with the photometric centers of gas and star emissions coinciding;
- (3) similar to stage 2, but the center of $H\alpha$ emission is shifted relative to the center of the stellar component emission;
- (4) a blue stellar condensation is observed in $UBVRI$, but no $H\alpha$ emission is present (see Gusev et al., 2023b, Fig. 1 for illustration). The first stage corresponds to a very young, highly dusty region with significant internal extinction. As extinction decreases, the SFR transitions to the second stage. The third stage occurs when the gas shell expands due to the explosions of the first supernovae. In the fourth stage, ionized hydrogen in the expanding shell recombines and cools. The emission centers of stars and gas are considered shifted if the angular distance between them exceeds $0.5''$.

This evolutionary morphological sequence pertains to low-mass SFRs, such as star clusters and associations. In star complexes, which are conglomerates of OB associations and clusters, the situation is more complex due to the potential presence of several SFRs of different ages. For them, we can only speak of a "photometric" age, where the latest star formation burst primarily contributes to its calculation. Our goal is to select regions where extinction measured by the Balmer decrement is from the same part of the SFR from which the main photometric flux originates. This goal is achieved for both large-scale SFRs, such as star complexes, and star associations (clusters).

Our study focuses on SFRs in the last three stages, selecting only those without $H\alpha$ emission (stage four) with a color index $(U - B)_0^i$, corrected for Galactic extinction and disk inclination extinction, not exceeding -0.537^m (see justification in Gusev et al., 2018). However, the "true" extinction of a young stellar cluster and, consequently, its luminosity, colors, mass, and age can only be determined in the second and fourth stages. In the second stage (class 2 in the catalog), as shown in Gusev et al. (2016, 2023b), extinction in the stellar system corresponds to extinction determined by the Balmer decrement. In the fourth evolutionary stage (class 0), excess extinction in the SFR is insignificant due to the dispersion of the gas-dust cloud; extinction in the star cluster (complex), which does not emit in $H\alpha$, is assumed to be $A_G + A_{\text{in}}$. In the third stage (class 1), the Balmer decrement provides extinction in the densest and brightest parts of the gas shell sur-

⁵ See <https://arca.sai.msu.ru/filters?ics=NBI> for details.

⁶ <http://stev.oapd.inaf.it/cgi-bin/cmd/>

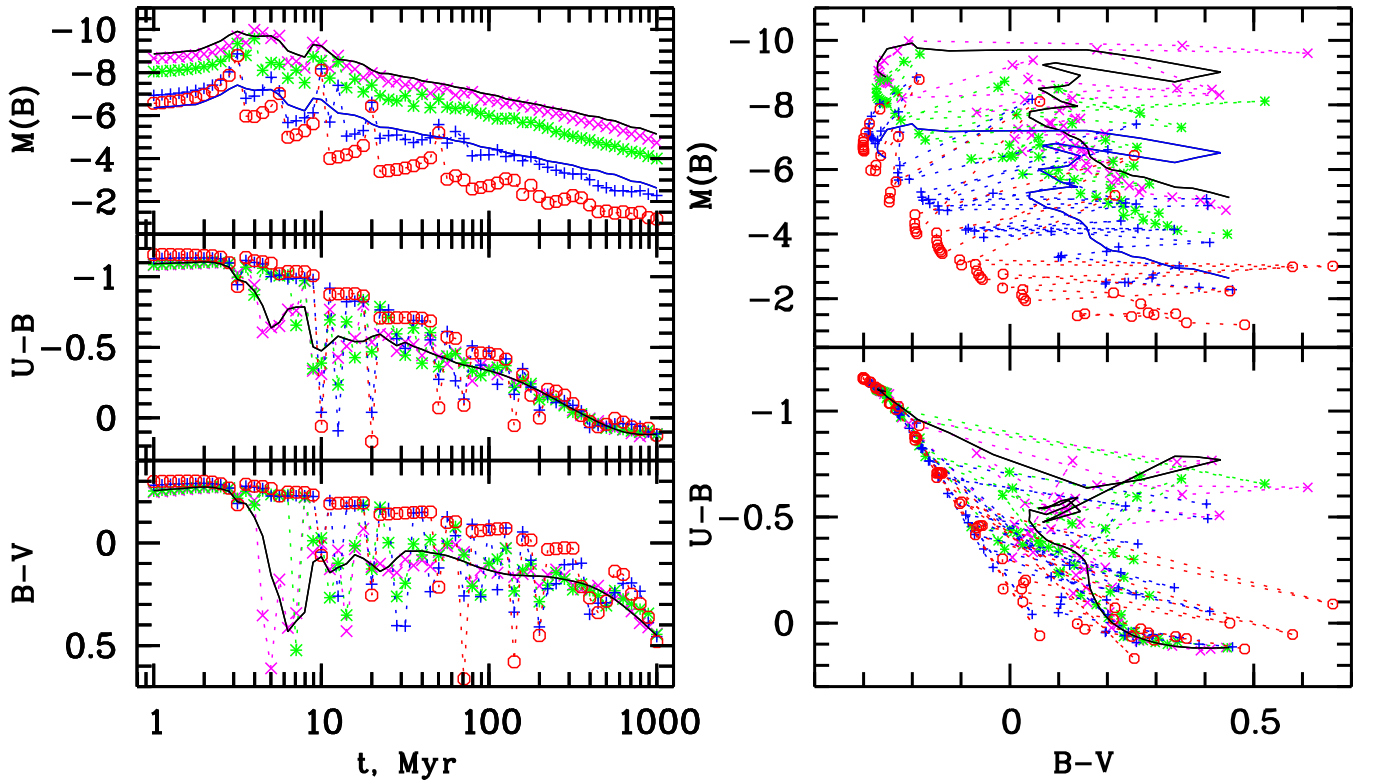


Fig. 2. Examples of evolutionary sequences from the standard mode of SSP models (continuously populated IMF) from the Padova stellar evolutionary track library CMD version 2.8 (Bertelli et al., 1994; Bressan et al., 2012; Tang et al., 2014) for stellar systems with metallicity $Z = 0.012$ and masses $1 \cdot 10^3 M_{\odot}$ (blue curves) and $1 \cdot 10^4 M_{\odot}$ (black curves) and the discrete mode of models (randomly populated IMF) for stellar systems with $Z = 0.012$ and masses $500 M_{\odot}$ (red circles connected by dashed lines), $1 \cdot 10^3 M_{\odot}$ (blue crosses connected by dashed lines), $5 \cdot 10^3 M_{\odot}$ (green stars connected by dashed lines) and $1 \cdot 10^4 M_{\odot}$ (purple diagonal crosses connected by dashed lines). The age range varies from 1 Myr to 1 Gyr. Shown are changes in absolute magnitude $M(B)$ and color indices $U - B$ and $B - V$ as functions of age (left), as well as the color-magnitude and two-color diagrams (right) for the model evolutionary sequences. The color indices for the standard mode models are independent of mass (blue and black curves overlap on the corresponding plots).

rounding the young star cluster (complex). It was shown in Gusev et al. (2016) that using the Balmer decrement to estimate stellar extinction in such objects gives an incorrect excess value A . Therefore, as shown below, we were able to estimate the mass for only 11 (age for 10) stellar clusters out of 33 SFRs with measured Balmer decrement (one of the HII regions in NGC 7292, studied in Gusev & Dodin, 2021, covers two star clusters). Additional five SFRs, for which mass and age estimates of the stellar component were obtained, are in the fourth evolutionary stage (not emitting in $H\alpha$). Since chemical composition data for them are absent, we used the average metallicity at the corresponding galactocentric distance obtained in Gusev et al. (2023a) when comparing them with evolutionary model grids.

3.2. Accounting for Stochastic Effects in the Initial Mass Function (IMF)

The second key aspect of the research methodology involves accounting for the stochastic effects in the discrete IMF, which is crucial for estimating the physical parameters of star clusters in SFRs. As demonstrated in Whitmore et al. (2010); Piskunov et al. (2011); Cerviño (2013), stochastic effects in a discretely and randomly populated IMF become significant for stellar systems with masses less than $5 \cdot 10^3 - 10^4 M_{\odot}$. In these cases, the luminosity of short-lived red giants can become comparable to the total luminosity of main-sequence stars. The main issue here is the uncertainty in the number and masses of massive main-sequence stars (see Figs. 2-4 for systems with a discrete IMF). Among the SFRs studied in this work, the effect of IMF discreteness is particularly important for young star clusters in the nearby galaxy NGC 7292.

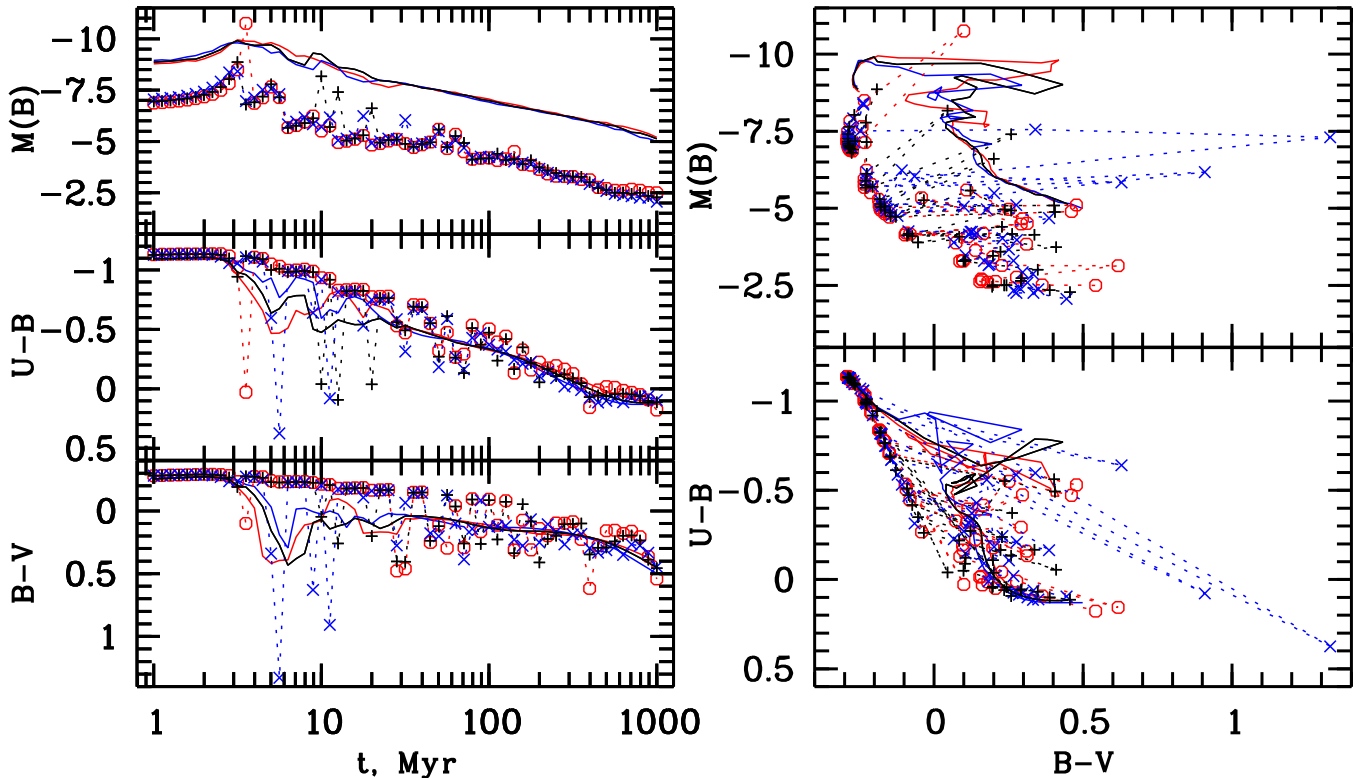


Fig. 3. The same as in Fig. 2, but for evolutionary sequences of varying metallicities. Examples include sequences from the standard mode models for stellar systems with mass $1 \cdot 10^4 M_{\odot}$ and $Z = 0.008$ (red curves), $Z = 0.012$ (black curves), and $Z = 0.018$ (blue curves), as well as from the discrete mode models for systems with mass $1 \cdot 10^3 M_{\odot}$ and $Z = 0.008$ (red circles connected by dashed lines), $Z = 0.012$ (black crosses connected by dashed lines), and $Z = 0.018$ (blue diagonal crosses connected by dashed lines).

A detailed description of the methodology for determining masses and ages using both continuously and stochastically populated IMFs is presented in Gusev et al. (2023b). In this section, we will discuss unpublished results comparing the evolutionary sequences of stellar systems for randomly and continuously populated IMFs, and provide a brief description of our approach.

Modern evolutionary models of stellar populations allow us to determine the physical properties of stellar populations in individual young star clusters using detailed grids of spectral energy distributions (SEDs) and model colors, each corresponding to a unique age, metallicity, and IMF of the stellar population.

To avoid ambiguity in the age-metallicity relation, a separate grid of single stellar population (SSP) models was constructed for each object studied here, with a fixed metallicity determined from independent spectroscopic observations (Gusev et al., 2016). Additionally, spectroscopic observations were used to calculate the Balmer decrement and estimate the interstellar extinction of the light emitted by the star cluster, allowing us to simultaneously account for the age-extinction relation that also affects the object’s position on color-color diagrams and, consequently, the age estimation of the stellar population

(Gusev et al., 2016). The spectroscopic data enabled us to account for the influence of the emission from the surrounding interstellar gas on the broadband photometry of young stellar populations (Gusev et al., 2016).

Taking these three factors into account allows for the comparison of the true integrated colors and luminosities of star groupings with model predictions. This comparison is made with fixed values for metallicity, stellar light extinction, and the contribution of gas emission to the integrated spectra of star groupings, which are determined from independent spectral observations, rather than leaving these values as free parameters. This approach requires a combination of photometric, $H\alpha$ spectrophotometric, and spectroscopic observations of young star groupings.

The ages and masses of the star cluster populations were determined by minimizing the deviation function calculated for each node of the model grid, comparing the true (corrected for extinction and gas emission) colors and luminosities of the star cluster with the grid of model colors calculated for the fixed metallicity from observations.

The colors of bright, massive star clusters ($M > 10^4 M_{\odot}$) were compared with models computed using a continuously populated IMF. In the case of less massive star clusters ($M < 10^4 M_{\odot}$) stochastic effects due to the

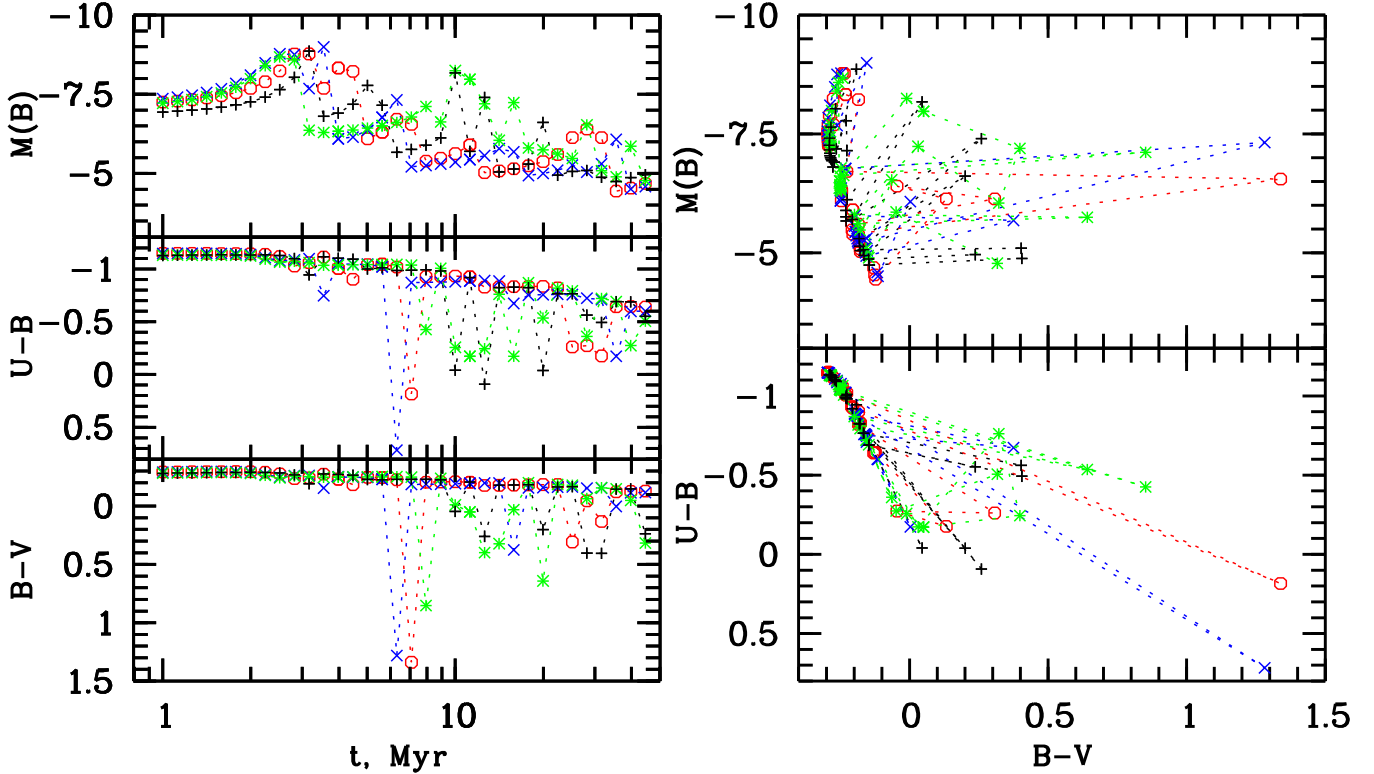


Fig. 4. The same as in Fig. 2, but for four randomly generated evolutionary sequences from the discrete mode of SSP models for systems with mass $1 \cdot 10^3 M_{\odot}$ and $Z = 0.012$ over an age range of 1 to 45 Myr.

discrete IMF significantly affect the cluster’s luminosity and color, especially in the long-wavelength part of the spectrum (Cerviño, 2013). Therefore, the colors and luminosities of low-mass star clusters were compared with models computed using a stochastically populated discrete IMF (Gusev et al., 2023b).

The discreteness of the IMF significantly affects the luminosity and colors of a cluster, which manifests as bursts and fluctuations in the evolutionary path of the photometric parameters of the cluster, caused by the appearance of red giants. There is also a systematic deviation between the photometric parameters (luminosity and color) of simple stellar population (SSP) models with discrete and continuous IMFs (Fig. 2). The luminosity evolution curves of discrete models exhibit sloping oscillations and consist of relatively short time intervals of recurring events. During one time interval, there is a slow, gradual increase in the cluster’s luminosity and an almost instantaneous burst, triggered by the evolution of the brightest main sequence star and its possible transformation into a bright, short-lived red supergiant. After the supergiant’s explosion, the process repeats with the evolution of the next brightest main sequence star and its transformation into a red giant. It should be noted that the deviations in the color and luminosity evolution curves of the discrete model, described above, are stronger in the case of low-mass clusters, where the number of red giants is small, and the

clusters spend most of the time as systems with main sequence stars. During bursts in low-mass clusters, the change in absolute stellar magnitude B can exceed 2^m , and the change in color can exceed 1^m . Moreover, in the framework of the discrete model, young low-mass stellar clusters ($M \leq 10^3 M_{\odot}$ younger than 30 Myr) are systematically bluer by $\sim 0.3 - 0.5^m$ in short-wavelength color indices than stellar systems of similar mass within the classical continuously populated IMF (see left graphs in Fig. 2); on the color-luminosity diagram, they are located to the left of the evolutionary tracks of stellar systems with a continuously populated IMF, and on the two-color diagram, they are to the left and above (see right graphs in Fig. 2). As the cluster mass increases to $1 \cdot 10^4 M_{\odot}$, the color and luminosity evolution curves of the discrete model converge to the curves of the standard continuous model (Fig. 2).

It should be noted that the differences between the model luminosities and color indices of stellar systems with different metallicities in the range of typical (solar and subsolar) Z are insignificant (Fig. 3) and generally do not exceed the characteristic measurement errors of the luminosities and color indices of real SFRs. Exceptions are the moments of bursts in low-mass stellar clusters (discrete IMF) and complexes with ages of 5-10 Myr (standard IMF). Extremely strong changes in the color indices $U - B$ and $B - V$ for a high-metallicity ($Z = 0.018$) stellar

system in the discrete IMF model in Fig. 3 (blue color) are not due to the large value of Z . A set of randomly generated models with a discrete IMF for systems with $Z = 0.012$, presented in Fig. 4, shows similar significant deviations for less metallic stellar systems. They occur in clusters and associations aged 5–10 Myr, at the same ages when the reddening and complex non-linear nature of the color index changes are also shown by models with a continuously populated IMF (Figs. 2, 3).

To construct the SSP model grid with a discrete IMF, the Monte Carlo method was used, generating random changes in the discrete IMF depending on the given mass of the model stellar cluster. For each given cluster mass, a discrete IMF was generated using a random number generator. With this random sampling, for a fixed value of the stellar system’s mass, the number of stars in the system was also fixed. At the next stage, using the randomly selected discrete IMF, the evolutionary sequence of 68 SSP models was calculated for each given cluster mass with a step of 0.05 dex in the interval $\log t = 5.9 - 9.3$ and a fixed metallicity Z , obtained from observations. For each calculation of the randomly selected discrete IMF, a random initial number was used, also obtained through a random number generator. When comparing the observed colors and luminosity of a given object with the model, 50 evolutionary sequences of discrete SSP models were used in each iteration. The number of iterations per object varied from 2 to 4. Thus, the number of simulations of the discrete IMF with random sampling per object ranged from 50 to 200. The total number of modeled models for each pair of mass and age estimates of the object ranged from 6800 to 13600.

To calculate the errors in age and mass estimates for the case of discrete IMF models based on the model colors corresponding to the chosen grid node with the minimum deviation functional value, the corresponding interval on the color evolution curve of the discrete model between two "red bursts" was selected, and the interpolation polynomial coefficients were calculated. Then, knowing the functional relationship between age and color, as well as the observational errors of the color indices, we obtained the accuracy of age estimates using the Gaussian formula for calculating the error of indirect measurements. Similarly, using the functional correlation between the model luminosity and the cluster mass in the interval between two "red bursts" and the observational errors of the objects’ integral luminosities, the mass estimate errors were determined.

A comparison of the mass and age estimates of GCs obtained using continuous and randomly populated IMFs for the same objects, conducted in Gusev et al. (2023b), showed that the mass and age estimates obtained within the discrete model are systematically larger, which is consistent with the systematic excess of luminosities of continuous IMF models over the luminosities of discrete models with the same stellar population masses (see Piskunov et al., 2011, Figs. 5 and 6). This difference de-

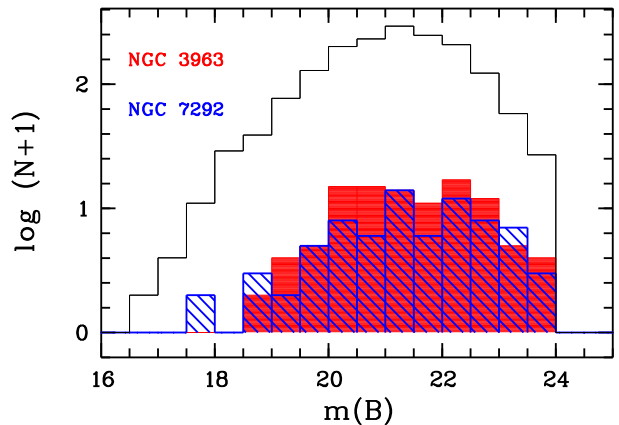


Fig. 5. Luminosity function for the complete sample of SFRs in the catalog (black histogram), regions in NGC 3963 (red), and regions in NGC 7292 (blue).

creases for high-mass ($M > 5 \cdot 10^4 M_{\odot}$) and very young ($t < 3$ Myr) or aging ($t > 50$ Myr) stellar groups.

4. RESULTS

4.1. Number of Identified SFRs, Their Sizes, and Locations in Galaxies

We have identified a total of 157 SFRs: 93 in the galaxy NGC 3963 and 64 in NGC 7292. Photometry was performed for all objects in the $UBVRI$ bands and in the $H\alpha$ ($H\alpha$ and $[NII]\lambda 6584$ separately for SFRs in NGC 3963, and $H\alpha + [NII]$ in NGC 7292), sizes were determined, and structures were described. Figure 5 shows the distribution of the identified SFRs by apparent stellar magnitude in the B band in comparison with the full sample of objects in the catalog. The number of studied SFRs in each galaxy is insufficient to determine the slope of the luminosity function and assess the completeness of the object sample. Assuming that the luminosity function follows a power law, we can qualitatively assess the completeness of the sample by the distribution peak of the regions in Fig. 5. Roughly, we estimate that our samples for NGC 3963 and NGC 7292 are complete at least up to $m(B) = 20^m$, which approximately corresponds to the limiting magnitudes to which the SFR samples are complete for most catalog galaxies (Fig. 5, see also Gusev et al., 2023b, Fig. 4 therein).

As explained in Section 3, estimating the mass and age of the stellar populations in the regions using our method is possible only for class 0 regions and those class 2 regions for which spectroscopic data are available. The number of SFRs satisfying these criteria is 16, with eight in each galaxy.

The galaxy NGC 7292 is the smallest in linear size among all 21 galaxies in the catalog. Consequently, all regions in it are located at galactocentric distances $r < 2$ kpc, comprising a significant portion of the regions close to the center of the entire catalog (see the left graph in

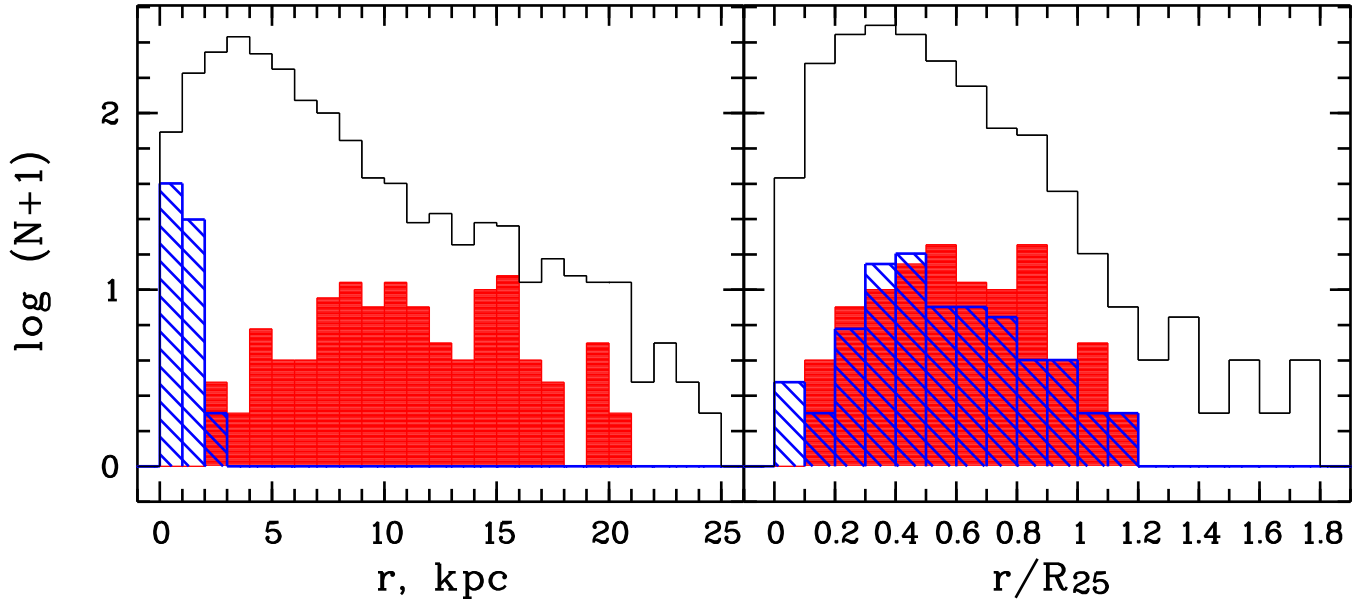


Fig. 6. Distribution of SFRs by absolute (left) and normalized to R_{25} (right) galactocentric distances. Notations are the same as in Fig. 5.

Fig. 6). In the large, massive NGC 3963, the SFRs are distributed over a wide range r , mainly concentrating in the spiral arms of the galaxy (Figs. 1, 6).

Despite significant differences in absolute values of r , the distributions of the regions by galactocentric distance normalized to the optical radius R_{25} in both galaxies are almost identical (right graph in Fig. 6), completely covering the range r within R_{25} .

Since NGC 3963 and NGC 7292 are located at substantially different distances from us (see Table 1), due to the hierarchical processes of star formation, we observe young regions in the nearby NGC 7292 with diameters of 40–125 pc (Fig. 7). The average value of $d = 75 \pm 20$ pc for the SFRs in NGC 7292 corresponds to the characteristic sizes of stellar associations (Efremov et al., 1987; Ivanov, 1991). The sizes of the SFRs in NGC 3963, ranging from 400 to 750 pc with an average of $d = 650 \pm 200$ pc (Fig. 7), are typical for stellar complexes (Efremov et al., 1987; Ivanov, 1991). It is worth noting that the largest SFRs in NGC 3963 with $d > 800$ pc are diffuse objects of relatively low surface brightness, possibly consisting of several complexes.

4.2. Gas Metallicity, Contribution of Its Emission to Total Luminosity in Broad Photometric Bands, and Morphology of Gas and Stellar Emission in SFRs

Differences in the masses of NGC 3963 and NGC 7292 significantly affect the variations in the chemical composition of their SFRs. The SFR metallicities were determined in our study Gusev et al. (2023b) using several

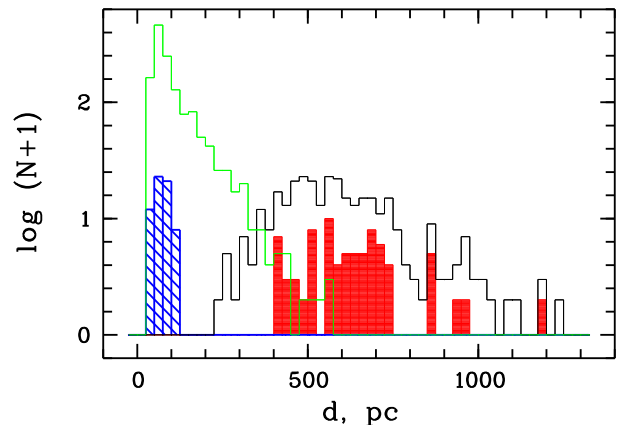


Fig. 7. Distribution of SFRs by size for objects in galaxies from the catalog located within 30 Mpc (green histogram) and beyond 30 Mpc from us (black histogram). Other notations are the same as in Fig. 5.

”strong line” methods (R (Pilyugin & Grebel, 2016), S (Pilyugin & Grebel, 2016), O3N2 (Pettini & Pagel, 2004), NS (Pilyugin & Mattsson, 2011), and HII-ChiMistry (Pérez-Montero, 2014)). For the HII regions in NGC 3963 and NGC 7292, the R method (using the lines [OII], [OIII], and [NII]) and the S method (using the lines [OIII], [NII], and [SII]) were employed (Gusev & Dodin, 2021). The SFR metallicity, Z , was determined from the oxygen abundance, O/H, as the arithmetic mean of the values obtained by both methods. In the giant massive galaxy NGC 3963, the SFR metallicity is average for the entire catalog sample, with its central metallicity being one of the highest

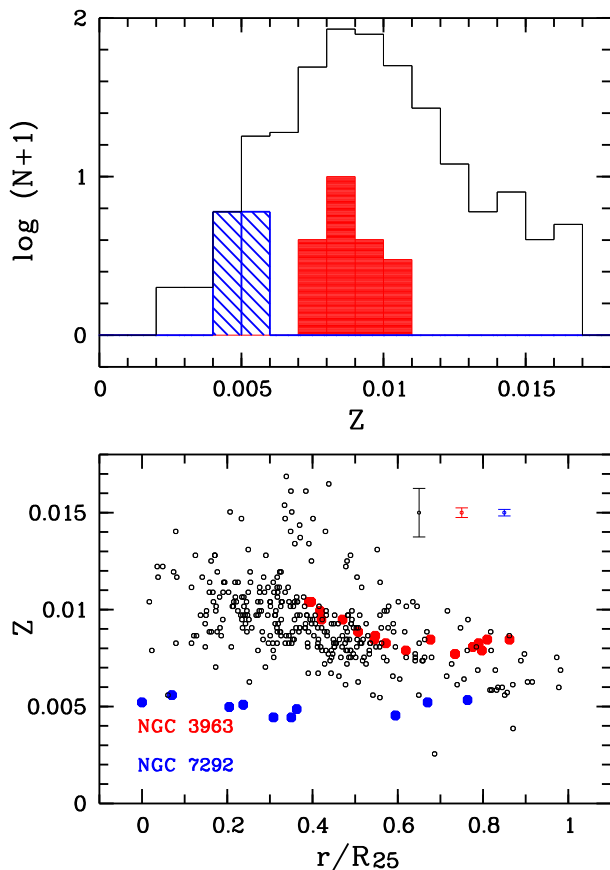


Fig. 8. Distribution of SFRs by metallicity (top; notations are the same as in Fig. 5) and radial distribution of SFRs by Z (bottom). Small black circles on the lower graph represent the complete sample of SFRs except for those with metallicity determined using the HII-ChiMistry method, red circles indicate SFRs in NGC 3963, and blue circles indicate SFRs in NGC 7292. Average measurement errors for Z in the SFR samples are shown in corresponding colors.

among the 21 galaxies in the sample (Fig. 8). In contrast, the small, low-mass NGC 7292 has the lowest metallicity of SFRs among all catalog galaxies (Fig. 8). It is also typical for irregular galaxies to lack a metallicity gradient (e.g., Richer & McCall, 1995; Hernández-Martínez et al., 2009).

It should be noted that the Z values obtained using all methods are consistent within the measurement errors (Gusev et al., 2023b), except for the HII-ChiMistry method, which systematically overestimates Z (see Gusev et al., 2023b, Fig. 7 therein). Therefore, the chemical composition parameters of the gas in the SFRs of NGC 3963 and NGC 7292 are not influenced by the calibration specifics of the methods used.

In Section 3, we highlighted the importance of studying the morphology of gas and stellar component emission in the $H\alpha$ line and broad photometric bands. Figure 9 shows the distribution of the studied SFRs by morpholog-

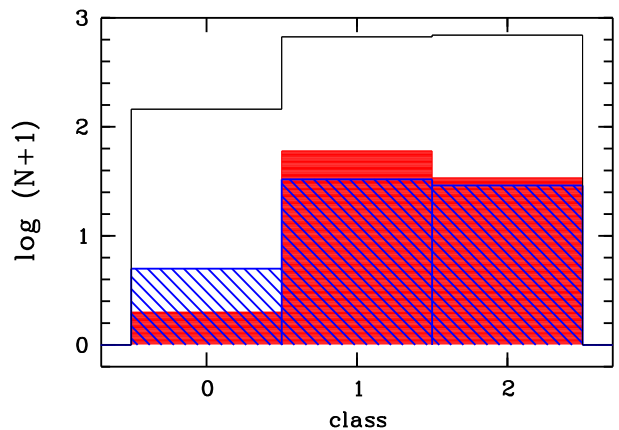


Fig. 9. Distribution of SFRs by gas and stellar emission morphology (see Section 3) for the complete sample of SFRs in the catalog galaxies with available $H\alpha$ line observations (classes 0-2; black histogram), SFRs in NGC 3963 (red), and SFRs in NGC 7292 (blue).

ical classes (evolutionary stages).⁷ As seen, the number of regions with coinciding and offset centers of gas emission and stellar radiation is approximately equal in both NGC 3963 and NGC 7292, as well as in the full sample. Given that our method for detecting young stellar groups and HII regions is independent of the morphological class of the SFRs (classification into classes occurs in subsequent stages), the approximate equality in the number of class 1 and class 2 regions is not a selection effect but reflects the roughly equal time spent by young stellar regions in these evolutionary stages. The number of class 0 regions (without $H\alpha$ emission) is 11% for the full sample of regions with known $H\alpha$ data (class 0–2 regions). In the galaxies studied here, there are only four such regions (6%) in NGC 7292 and one (1%) in NGC 3963 (Fig. 9).

Gusev et al. (2023b) found that a significant (more than 10%) portion of SFRs has a gas emission contribution exceeding 40% in the photometric B band. Among the regions in NGC 3963 and NGC 7292, no objects with such a high gas emission contribution were found: in most SFRs, this contribution does not exceed 15%. However, in the SFRs of NGC 7292, the gas emission contribution in the B band (average 12%, maximum 35%) is systematically higher than in the SFRs of NGC 3963 (average 5%, maximum 22%). For class 2 regions, the data on gas contribution are presented in Table 3.

4.3. Photometric Parameters of SFRs

The positions of the studied SFRs on two-color diagrams are shown in Figs. 10 and 11. Figure 10 presents the color indices of the SFRs corrected for Galactic extinction and extinction associated with the inclination of the galactic

⁷ In Gusev et al. (2023b), 341 class 2 objects with no Balmer decrement measurements were erroneously assigned to class 1. In this paper, we correct this error.

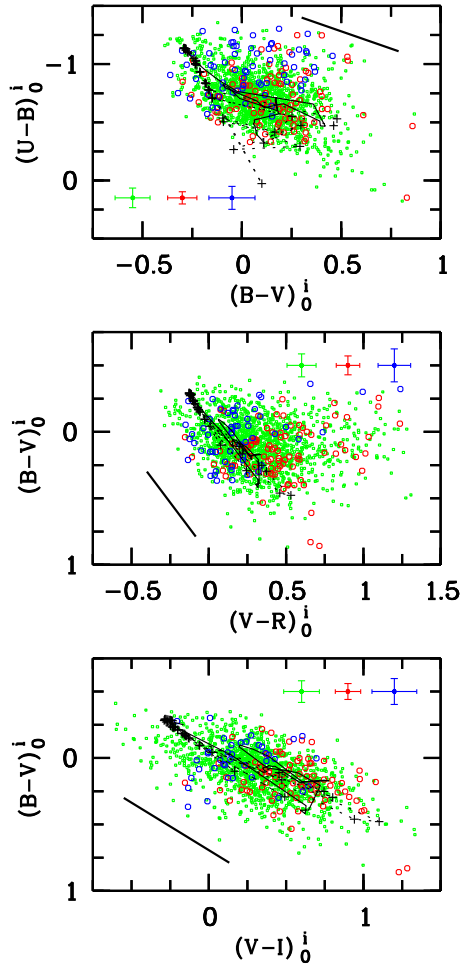


Fig. 10. Two-color diagrams $(U - B)_0^i - (B - V)_0^i$, $(B - V)_0^i - (V - R)_0^i$, and $(B - V)_0^i - (V - I)_0^i$. Shown are SFRs with color indices corrected for galactic extinction A_G and extinction caused by the galaxy disk inclination, A_{in} . Green dots represent SFRs from the catalog by Gusev et al. (2023b), red circles denote SFRs in NGC 3963, and blue circles denote SFRs in NGC 7292. Average measurement errors for color indices are shown with corresponding color error bars. Black curves represent evolutionary tracks for a stellar system with a continuous IMF and $Z = 0.008$ in the age range t of 1 to 100 Myr; black crosses connected by dashed lines show an example of an evolutionary sequence for a stellar system with a randomly populated IMF with mass $M = 5 \cdot 10^3 M_\odot$ and $Z = 0.008$ in the range t from 1 to 100 Myr. Black thick segments in the corners of the diagrams are parallel to the reddening vector.

disks. Although the actual extinction in SFRs typically exceeds the sum of extinctions $A_G + A_{in}$ (Gusev et al., 2023b), and accounting for gas contribution can shift SFRs away from the reddening vector (see Gusev et al., 2016, Fig. 12 therein), the majority of catalog objects are compactly located on the diagrams – within areas correspond-

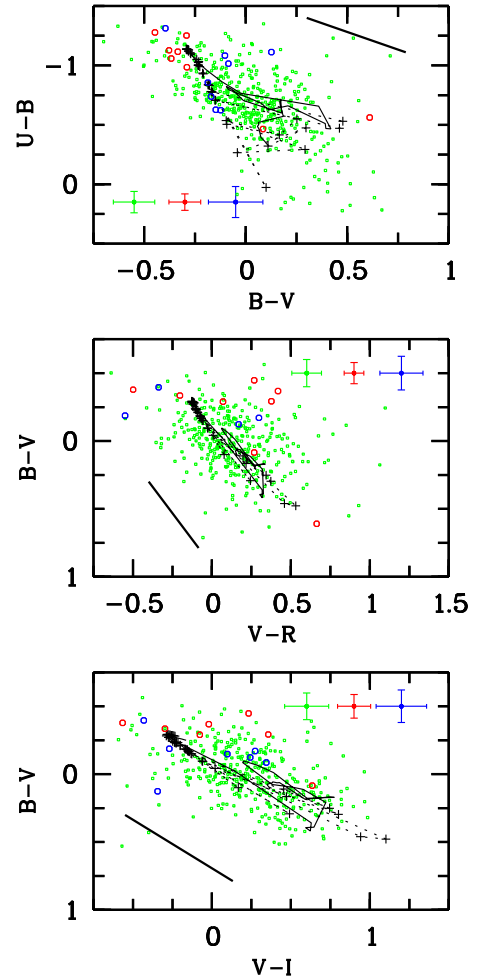


Fig. 11. The same as in Fig. 10, but for the "true" color indices of the stellar population in SFRs corrected for the contribution of gas and extinction calculated from the Balmer decrement. Notations are the same as in Fig. 10.

ing to young stellar systems with continuous or discrete star formation histories (Fig. 10). An exception is the $(B - V)_0^i - (V - R)_0^i$ diagram, where SFRs with very high color indices $(V - R)_0^i$ up to 1.2 – 1.3 are observed. This is due to the significant contribution of gas to the flux in the R band (Gusev et al., 2023b). The objects in NGC 3963 and NGC 7292 studied in this work do not stand out among the SFRs of the full catalog sample on the diagrams in Fig. 10.

On the diagrams in Fig. 11, where the colors of objects are corrected for gas contribution and extinction obtained from the Balmer decrement, the cloud of points representing color indices also concentrates along model evolutionary tracks. The degree of concentration is lower than on the diagrams in Fig. 10, which is explained by the smaller number of objects (only class 0 and class 2 SFRs with known Balmer decrement) and larger measurement errors of the "true" color indices. On the $(B - V) - (V - R)$ diagram, the group of objects with extremely high $V - R$

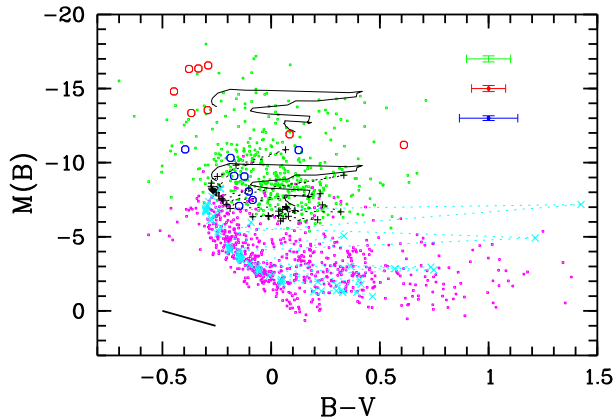


Fig. 12. The color-luminosity diagram for the "true" absolute stellar magnitudes $M(B)$ and color indices $B - V$ of the stellar population in SFRs in the galaxies. Purple points represent open star clusters in our Galaxy from the catalog of Kharchenko et al. (2009). Cyan crosses connected by dashed lines show an example of an evolutionary sequence for a stellar system with a randomly populated IMF with mass $M = 500M_{\odot}$ and $Z = 0.018$ in the range t from 1 Myr to 1 Gyr. Black curves indicate the evolutionary tracks for a stellar system with a continuous IMF, with masses $M = 1 \cdot 10^6 M_{\odot}$ (upper curve) and $M = 1 \cdot 10^4 M_{\odot}$ (lower curve) and $Z = 0.008$ in the age range t from 1 to 100 Myr. Other notations are the same as in Fig. 10.

values disappears, which may indicate correct accounting of gas contribution to the fluxes in the photometric bands.

It is noteworthy that on the $(U - B) - (B - V)$ diagram, most SFRs from NGC 3963 are located in the upper left corner of the diagram representing the region of the youngest stellar populations. In contrast, half of the eight regions in the nearby galaxy NGC 7292 have color indices corresponding to stellar systems with discretely populated star formation histories during periods without outbursts (stars in the stage of red (super)giants; Figs. 2-4, 11).

As indicated in Section 3, the physical parameters of SFRs were evaluated using two color indices: $U - B$ and $B - V$. SFRs in the R and I bands are distinguished much worse than in the shorter wavelength bands. In some cases, we were even unable to obtain photometry with satisfactory accuracy, which is why the number of SFRs on the $(B - V) - (V - R)$ and $(B - V) - (V - I)$ diagrams is lower than on the $(U - B) - (B - V)$ diagram (Fig. 11). In addition, fluxes in R and I are weakly sensitive to changes in age in young stellar systems and, conversely, are more sensitive to the possible presence of old stellar populations (e.g., due to non-simultaneous or repeated star formation outbursts, poorly described by SSP models). For fluxes in the R band, another factor is the large contribution of gas emission to the total flux. Errors in spectroscopic data give additional uncertainty to measurements in R . Consequently, there is a significant lack of agreement with models for a considerable number of studied SFRs on the

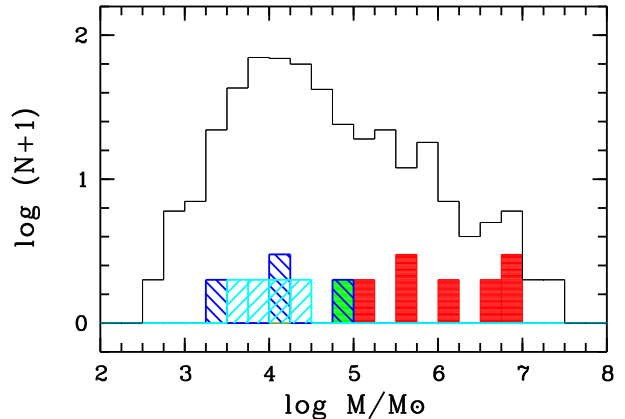


Fig. 13. Distribution of SFRs by mass for the complete catalog sample (black histogram), class 2 SFRs in NGC 3963 (red), class 0 SFRs in NGC 3963 (green), class 2 SFRs in NGC 7292 (blue), and class 0 SFRs in NGC 7292 (cyan).

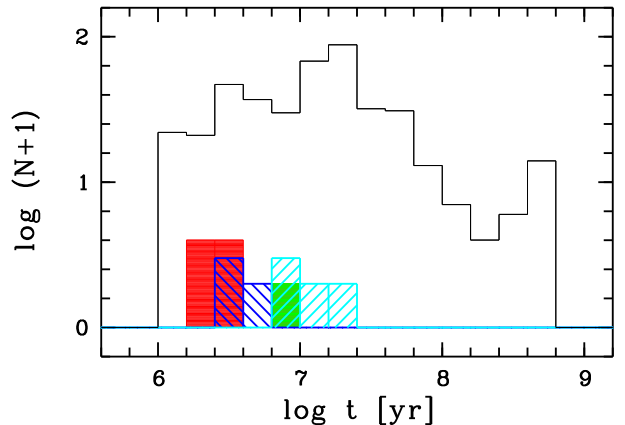


Fig. 14. Distribution of SFRs by age. Notations are the same as in Fig. 13.

$(B - V) - (V - R)$ and $(B - V) - (V - I)$ diagrams (Fig. 11). It is also noted that stochastic effects in star formation histories manifest in longer wavelength bands for larger stellar systems compared to shorter wavelength bands U , B , V (Cerviño, 2013).

On the color-luminosity diagram (Fig. 12), in addition to the objects in our catalog, we show the positions of open star clusters in our Galaxy from catalog of Kharchenko et al. (2009). SFRs in NGC 3963 and NGC 7292 do not stand out from the objects in the full catalog sample on this diagram. We observe high-mass stellar complexes in the distant NGC 3963 as expected, while in the nearby NGC 7292, relatively low-mass stellar associations are observed (Fig. 12). The least massive SFRs in NGC 7292 correspond in luminosity to the most massive open star clusters in the Galaxy (Fig. 12).

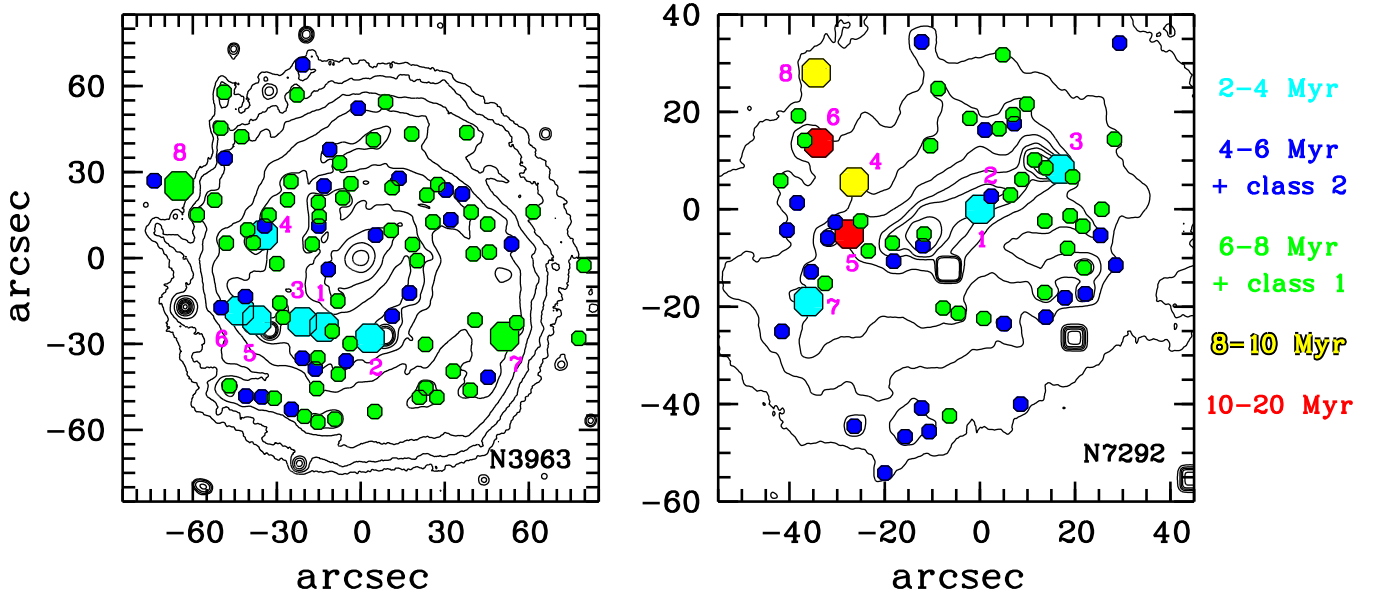


Fig. 15. Distribution of SFRs of different ages and evolutionary classes in the galaxies NGC 3963 (left) and NGC 7292 (right). Large circles denote SFRs with measured age estimates, while small circles represent other SFRs of classes 1 and 2. Purple numbers correspond to the SFRs listed in Table 4.

4.4. Estimates of the Mass and Age of the Stellar Component of Star Formation Regions

The range of stellar population masses in SFRs in the galaxy NGC 7292, $M = 3 \cdot 10^3 - 6 \cdot 10^4 M_{\odot}$, corresponds to typical masses for objects in the catalog (Fig. 13). The most massive complexes in NGC 3963 reach $8 \cdot 10^6 M_{\odot}$, making them some of the most massive SFRs among all objects in the catalog (Fig. 13). Only the largest complexes in NGC 2336, NGC 5351, and NGC 7678 have larger masses (Gusev et al., 2023b).

It should be noted that SFRs without emission in the $H\alpha$ line (class 0) are generally less massive in both galaxies (in NGC 7292, class 0 objects have an average mass $M = (1.0 \pm 0.7) \cdot 10^4 M_{\odot}$ with a median value $M = 0.64 \cdot 10^4 M_{\odot}$, compared to an average mass $(2.3^{+2.4}_{-2.3}) \cdot 10^4 M_{\odot}$ and median mass of $1.4 \cdot 10^4 M_{\odot}$ for class 2 objects; the single class 0 object in NGC 3963 was the least massive among the eight SFRs with measured mass). This can be explained by selection effects: for comparable apparent magnitudes, the extinction in regions with gas emission is on average higher by $\sim 2^m$ in the B band. A small decrease in luminosity with age does not compensate for the effect of excessive extinction. An exception is the least massive HII region in NGC 7292, which also has the highest $m(B)$ value among the eight regions with mass estimates in the galaxy. This object was not identified by the SExtractor software and was included in our sample due to a more thorough search in photometric bands for HII regions studied in Gusev & Dodin (2021).

Among the 16 SFRs with mass estimates, the age of the stellar population could be determined for 15. For one

region in NGC 7292, the error in age t estimation was too large for any qualitative analysis. The distribution of SFRs by age is shown in Fig. 14. With a full range of measured ages from 2.2 to 18 Myr, only two regions in NGC 7292 have $t > 10$ Myr. On average, complexes in NGC 3963 show younger ages: six out of eight SFRs in the galaxy are younger than 3 Myr, and the other two are younger than 8 Myr. In NGC 7292, we did not find any stellar associations younger than 3.1 Myr.

The difference in ages of SFRs is due to the fact that a significant proportion of studied objects in NGC 7292 do not have emission in $H\alpha$ (are not HII regions). As mentioned in Section 3, classes 0 and 2 represent different evolutionary stages of SFRs. The distribution in Fig. 14 clearly shows this: the ages of HII regions range from 2.2 to 7.9 Myr, while regions without gas emission have ages t from 6.3 to 18 Myr. This separation provides additional support for the validity of our age t estimates.

The distribution of SFRs of different ages in galaxies is shown in Fig. 15. The age of objects for which we could not estimate t can be roughly inferred from their morphological class – a marker of evolutionary development of SFRs (see Section 3). The age boundary between classes 1 and 2 is approximately 4–5 Myr (Whitmore et al., 2011). Such objects are marked with small circles in Fig. 15, and their color approximately corresponds to the color of SFRs of the corresponding age (see the legend on the right side of the figure).

In the galaxy NGC 3963, SFRs younger than 6 Myr are mostly located in the spiral arms of the inner disk. In the outer part of the distorted southern spiral (Figs. 1, 15), which is apparently influenced by the neighboring galaxy

Table 3. Photometric parameters of SFRs

N	NGC	Coordinates	$m(B)$, mag	$M(B)$, mag	$U - B$	$B - V$	Gas contribution
1528	3963	13.1''E, 24.1''S	21.40 ± 0.02^m	-14.90 ± 0.09^m	-1.28 ± 0.03	-0.45 ± 0.04	0.14
1531	3963	3.3W, 28.0S	20.05 ± 0.03	-16.56 ± 0.06	-0.98 ± 0.04	-0.29 ± 0.04	0.06
1532	3963	20.9E, 22.3S	21.30 ± 0.02	-16.32 ± 0.23	-1.13 ± 0.05	-0.38 ± 0.06	0.03
1540	3963	34.8E, 8.0N	23.30 ± 0.07	-13.35 ± 0.24	-1.06 ± 0.10	-0.37 ± 0.12	0.22
1556	3963	37.2E, 21.7S	20.27 ± 0.02	-16.35 ± 0.06	-1.12 ± 0.03	-0.33 ± 0.03	0.08
1564	3963	43.4E, 18.4S	22.57 ± 0.13	-13.54 ± 0.86	-1.25 ± 0.23	-0.29 ± 0.28	0.12
1576	3963	51.3W, 27.4S	21.69 ± 0.03	-11.91 ± 0.07	-0.46 ± 0.04	0.08 ± 0.05	0.03
1597	3963	64.9E, 25.2N	22.52 ± 0.01	-11.20 ± 0.01	-0.56 ± 0.02	0.61 ± 0.02	0
1604	7292	0.0, 0.0	20.53 ± 0.14	-10.32 ± 0.20	-0.86 ± 0.19	-0.19 ± 0.21	0.09
1605	7292	2.4W, 2.7N	21.28 ± 0.14	-10.89 ± 0.34	-1.31 ± 0.19	-0.40 ± 0.18	0.06
1617	7292	16.8W, 8.3N	19.78 ± 0.04	-10.85 ± 0.05	-1.11 ± 0.06	0.13 ± 0.05	0.35
1637	7292	26.4E, 5.6N	22.05 ± 0.09	-7.48 ± 0.09	-1.02 ± 0.10	-0.09 ± 0.12	0
1642	7292	27.5E, 5.1S	20.43 ± 0.05	-9.10 ± 0.05	-0.74 ± 0.06	-0.17 ± 0.08	0
1647	7292	33.9E, 13.6N	22.45 ± 0.11	-7.08 ± 0.11	-0.63 ± 0.19	-0.15 ± 0.16	0
1657	7292	36.0E, 18.9S	22.86 ± 0.19	-8.06 ± 0.25	-1.08 ± 0.23	-0.10 ± 0.23	0.24
1658	7292	34.4E, 28.0N	20.46 ± 0.01	-9.07 ± 0.01	-0.62 ± 0.02	-0.12 ± 0.03	0

Table 4. Physical and chemical parameters of SFRs

NGC	No.	Z	d , pc	M , $10^4 M_\odot$	t , Myr
3963	1	0.010	520	180 ± 10	2.2 ± 2.1
3963	2	0.010	700	540 ± 10	2.8 ± 0.4
3963	3	0.009	640	730 ± 10	$2.2^{+3.2}_{-2.2}$
3963	4	0.009	420	37 ± 2	$2.5^{+2.8}_{-2.5}$
3963	5	0.008	850	800 ± 40	$2.2^{+2.3}_{-2.2}$
3963	6	0.008	570	34 ± 2	2.8 ± 2.4
3963	7	0.008	660	14 ± 1	7.9 ± 1.0
3963	8	–	560	6.3 ± 0.5	6.3 ± 0.2
7292	1	0.005	75	1.4 ± 0.2	3.2 ± 0.7
7292	2	0.006	75	5.8 ± 0.4	–
7292	3	0.004	65	1.7 ± 0.1	3.2 ± 0.1
7292	4	–	80	0.64 ± 0.04	8.9 ± 0.5
7292	5	–	90	2.0 ± 0.1	13 ± 3
7292	6	–	90	0.35 ± 0.04	18 ± 4
7292	7	0.005	115	0.26 ± 0.04	4.0 ± 0.1
7292	8	–	125	1.00 ± 0.04	8.9 ± 0.2

NGC 3958 (van Moorsel, 1983), the majority of complexes belong to class 1, and the only complex with an estimated has an age of 7.9 Myr.

In NGC 7292, the youngest regions ($t < 4$ Myr or class 2) are located in the center of the bar, near the ends of the bar (but not in the brightest regions at the ends), as well as on the southern and eastern outskirts of the disk (Fig. 15). It is noted that in large stellar complexes both at the eastern and western ends of the bar, relatively older bright SFRs are located in the center of the stellar complex (green circles on the map), while younger SFRs are on its periphery (cyan and blue circles). Within stellar complexes in the galaxy, reaching 350-400 pc in diameter, close SFRs with relatively large age differences, up to 10-12 Myr, are observed. This results from non-simultaneous star formation in large stellar complexes. The typical du-

ration of star formation on scales of ~ 300 pc is about 20 Myr (see Efremov & Elmegreen, 1998, Fig. 8 therein). In NGC 5585, which is similar in mass and luminosity to NGC 7292 and has low surface brightness, the typical age difference between SFRs located 100 pc apart is also ≈ 10 Myr (see Gusev & Shimanovskaya, 2019, Fig. 9 therein). The brightest dynamically prominent HII region in NGC 7292, located at the eastern end of the bar and previously thought to be the center of the galaxy, was examined by us in detail (see Gusev et al., 2023a, Fig. 8 therein). Its age was estimated in Gusev et al. (2023a) to be 6-8 Myr.

Tables 3 and 4 provide information on the 16 SFRs in the galaxies for which physical parameters of the stellar population were estimated. Table 3 lists the catalog number N , coordinates in arcseconds relative to the center, apparent ($m(B)$) and "true" absolute stellar magnitudes ($M(B)$), "true" color indices $U - B$ and $B - V$, and the contribution of gas to the total flux in the band. Table 4 presents the object number from Fig. 15, gas metallicity Z , SFR size d , mass M , and age t of the stellar population. A gas contribution of 0 in Table 3 and absence of data on Z in Table 4 indicate the lack of emission in the $H\alpha$ line (evolutionary class 0). Complete data on the parameters of these and other 141 SFRs in NGC 3963 and NGC 7292 are provided in version 3 of our catalog.⁸

5. DISCUSSION OF THE RESULTS

In this section, we will examine some general dependences for all objects in the catalog, which have both fundamental and methodological significance.

One possible indicator of the age of HII regions is the equivalent width of the Balmer hydrogen emission lines (Copetti et al., 1986). In Gusev et al. (2018), we intro-

⁸ http://lnfm1.sai.msu.ru/~gusev/sfr_cat.html

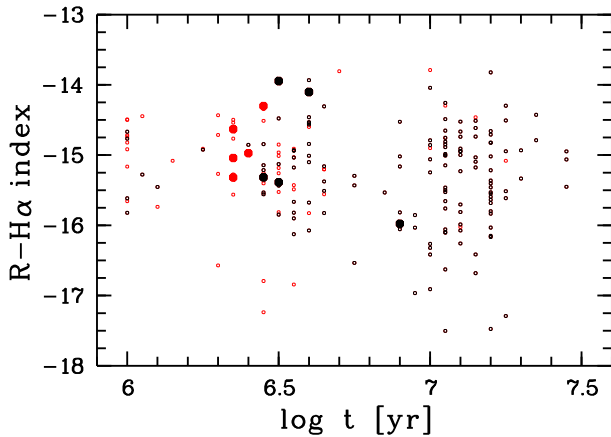


Fig. 16. Relationship between the age of the stellar population in SFRs and the $R - H\alpha$ index. Small circles are objects from the catalog of Gusev et al. (2023b), large circles are objects in NGC 3963 and NGC 7292. Black denotes SFRs with an age estimation error $\Delta \log t < 0.2$ dex, while red indicates those with an error greater than 0.2 dex.

duced the index $R - H\alpha = R + 2.5 \log F(H\alpha + [NII])$, where R is the apparent stellar magnitude in the R band, and $F(H\alpha + [NII])$ is the flux in $\text{erg}\cdot\text{cm}^{-2}$, which can serve as a replacement for $\text{EW}(H\alpha)$ (see Gusev et al., 2023b, Fig. 17 therein). It should be noted that for NGC 3963 – the only galaxy out of the 21 in the catalog for which separate flux measurements were made for the $H\alpha$ and $[NII]\lambda 6584$ lines, we calculated the $R - H\alpha$ index as $R + 2.5 \log[F(H\alpha) + F(1.33[NII]\lambda 6584)]$, where coefficient 1.33 reflects the contribution of emission in the $[NII]\lambda 6548$ line.

Figure 16 shows the dependence between the age of an SFR and the $R - H\alpha$ index. We used the $R - H\alpha$ index instead of $\text{EW}(H\alpha)$ due to greater uniformity in measurements of $R - H\alpha$. The $\text{EW}(H\alpha)$ value is sensitive to the choice of the background area subtracted from the spectrum continuum, and in the case of slit spectroscopy, it can also be affected by the inhomogeneity of the emission distribution in $H\alpha$ and the stellar continuum within the SFR. Criticism of using parameter $\text{EW}(H\alpha)$ as an age indicator can be found in Morisset et al. (2016); Kreckel et al. (2022); Scheuermann et al. (2023).

Unlike the similar plot in Gusev et al. (2023b), Fig. 16 presents objects with any errors in the estimate of t ; regions with $\Delta \log t > 0.2$ dex are highlighted in red. Large circles denote 10 objects of class 2 with age estimates from galaxies investigated in this study. As seen from the figure, including new data does not change the conclusions drawn in Gusev et al. (2023b): while the minimum value of the $R - H\alpha$ index for SFRs of the corresponding age decreases with increasing t (from ≈ -16 for $t \approx 2$ Myr to ≈ -17.5 for $t \approx 12$ Myr), the upper limit of $R - H\alpha \approx -14$ (corresponding to $\text{EW}(H\alpha) \sim 1000\text{\AA}$) does not depend on the age of the SFR. Thus, $R - H\alpha$ index and $\text{EW}(H\alpha)$ are poor indicators of the age of young stellar systems. The

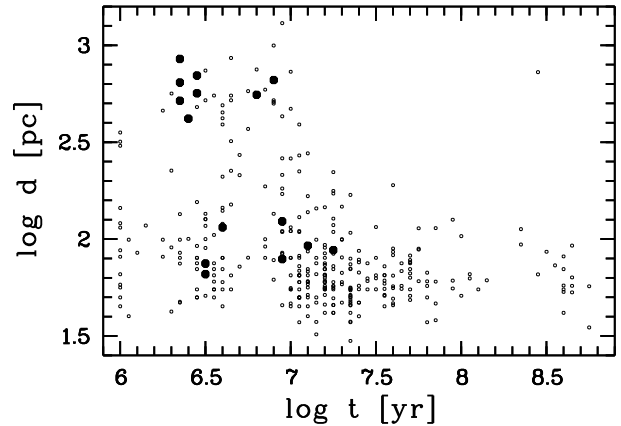


Fig. 17. Size–age relationship for SFRs from the complete catalog sample (small circles) and regions in NGC 3963 and NGC 7292 (large black circles). Multi-component SFRs (e.g., double, triple) are not shown on the plot.

only conclusion possible from the analysis of Fig. 16 is that the index $R - H\alpha < -16$ ($\text{EW}(H\alpha) < 100\text{\AA}$) indicates an age of the SFRs greater than 3 Myr.

Among the SFRs in our sample, there are both large star complexes and aggregates – compound systems including groups of OB associations and young clusters – and individual star associations and clusters. Gravitationally unbound star associations expand with age (Efremov & Elmegreen, 1998; Portegies Zwart et al., 2010). The sizes of young clusters are weakly dependent on age. The linear resolution of our observations, even in the nearest galaxies, is 30–40 pc and does not allow us to detect more compact star clusters. Differentiating the youngest stellar systems ($t < 10$ Myr) by parameters into associations and clusters is difficult in principle (Gieles & Portegies Zwart, 2011), and with our linear resolution, it is impossible.

The position of the studied SFRs on the size–age diagram (Fig. 17) illustrates the presence of various types of young stellar objects and their characteristics. A group of large star formation complexes ($d > 400$ pc), including NGC 3963, stands out, and almost all of them are younger than 10 Myr. This is a consequence of two main factors. First, star complexes, with very rare exceptions, are relatively short-lived formations, disintegrating within 100–200 Myr (Efremov, 1995). Second, star formation in them does not occur simultaneously. The photometric age estimate of a complex is mainly influenced by the most recent star formation bursts in its components. Selection effects must also be considered: most SFRs were identified based on emission in the $H\alpha$ line.

Most SFRs with diameters up to 100 pc and older than 10 Myr are apparently young star clusters. In Fig. 17, no dependency between age and size is observed for them. Note the absence of compact objects with $d < 80$ pc among SFRs aged 4–8 Myr. HII regions of this age are in the phase of expanding ionized gas envelopes, whose

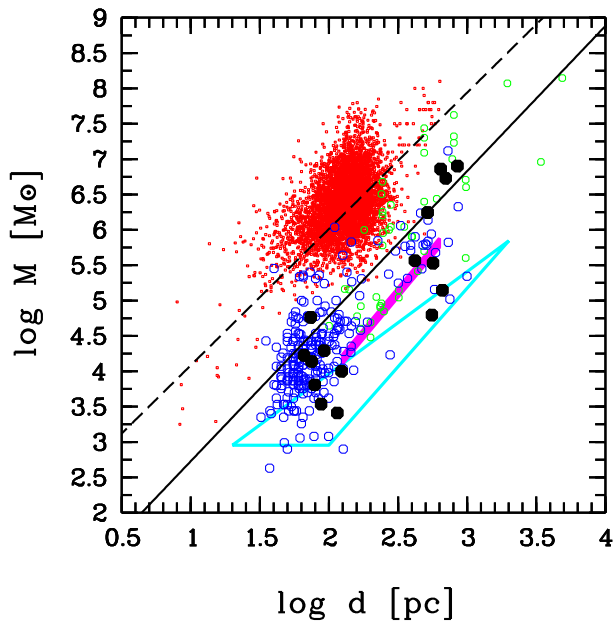


Fig. 18. Mass–size relationship for GMCs (red dots from Bolatto et al., 2008; Wei et al., 2012; Rosolowsky et al., 2021) and SFRs (green circles (Adamo et al., 2013), purple parallelogram (Bastian et al., 2005), region within the cyan triangle from Gouliermis et al. (2017)). Blue circles represent single SFRs from our catalog (Gusev et al., 2023b) with $\Delta M/M < 0.2$; black circles represent SFRs in NGC 3963 and NGC 7292. The solid black line represents the $M \sim d^{2.0}$ relationship for young massive star clusters according to Adamo et al. (2013); the dashed black line represents the $M \sim d^{1.9}$ relationship for GMCs according to Bolatto et al. (2008); Adamo et al. (2013).

emission contributes to the total flux in photometric bands U , B , and others. The sizes of SFRs at this evolutionary stage, as determined from our images in the band, are effectively the sizes of the expanding gas envelopes.

The mass–size dependences for SFRs and their progenitors – giant molecular clouds (GMCs) – also have significant fundamental importance. The correlation $M \sim d^2$ between the masses and sizes of GMCs has been known since Larson (1981). A close relationship between M and d was also obtained for SFRs: $M \sim d^{2.33 \pm 0.19}$ (Bastian et al., 2005), $M \sim d^{2.0 \pm 0.3}$ (Adamo et al., 2013). Although recent studies show more complex relationships between masses and sizes in both gas and stellar conglomerates (see review in Grudić et al., 2021), the dependence $M \sim d^2$ for GMCs and SFRs is well explained within modern interstellar medium physics theories. The shift of ~ 1.5 dex between the relationships for GMCs and SFRs is explained by the inefficiency of star formation ($< 10\%$) in GMCs (Larson, 1981; Bastian et al., 2005; Adamo et al., 2013).

Figure 18 shows the mass–size diagram for numerous samples of GMCs (Bolatto et al., 2008; Wei et al., 2012; Rosolowsky et al., 2021) and HII regions (Bastian et al., 2005; Adamo et al., 2013; Gouliermis et al., 2017). Unlike

Fig. 20 in Gusev et al. (2023b), where we included only isolated single SFRs from our catalog, here we also added single objects – parts of larger SFRs. The mass–size plot shows that the positions of SFRs in our sample (blue and black circles) best match the results of Adamo et al. (2013) (green circles), extending their dependence for complexes toward smaller star associations. Our results for some catalog objects are not inconsistent with data from Bastian et al. (2005) (purple parallelogram) and Gouliermis et al. (2017) (cyan triangle). However, effects related to the linear resolution of our observations play a significant role here: for SFRs with diameters smaller than the resolution limit, the d value is overestimated and equals the linear resolution for the corresponding galaxy. This effect is clearly visible in the case of SFRs from NGC 3963 and NGC 7292 (black circles in Fig. 18), which do not show any dependence of M on d separately for SFR samples in distant NGC 3963 (upper right group of black circles in the figure) and nearby NGC 7292 (lower left group).

6. CONCLUSIONS

In this study, we present results from investigating the physical parameters of stellar populations in 93 SFRs of the large spiral galaxy NGC 3963 with signs of peculiarity and 64 SFRs in the Magellanic-type galaxy NGC 7292. The data obtained complement our research in Gusev et al. (2023b), which studied 1510 SFRs in 19 galaxies, and are included in the third version of the catalog of photometric, physical, and chemical parameters of SFRs, available electronically on the website of the SAI MSU (http://lnfm1.sai.msu.ru/~gusev/sfr_cat.html).

We focus on two key aspects of the methodology for estimating the age and mass of SFRs using stellar population evolutionary models:

- (1) The use of the extinction measure in SFRs determined from the Balmer decrement is only accurate for HII regions where the photometric centers of the gas emission (in the $H\alpha$ line) and the stars (in broad photometric bands) coincide.
- (2) For analyzing stellar systems with masses less than $1 \cdot 10^4 M_{\odot}$, it is necessary to use evolutionary models with a discrete (randomly populated) IMF.

Among the 157 identified SFRs in the galaxies, we were able to obtain metallicity estimates for 27, extinction measurements from the Balmer decrement for 33, mass estimates for 16, and age estimates for 15 SFRs.

The main findings of the study are as follows.

- (1) The number of HII regions with coinciding and shifted centers of gas and stellar emission is approximately equal. This likely reflects the approximate equality in the time that a young stellar region spends at corresponding evolutionary stages.
- (2) The diameter of SFRs in NGC 3963, 650 ± 200 pc, is typical for star complexes, while in NGC 7292, 75 ± 20 pc, it is typical for star associations.
- (3) The stellar population masses in the studied SFRs in

the galaxy NGC 3963 range from $6 \cdot 10^4 M_{\odot}$ to $8 \cdot 10^6 M_{\odot}$, while in the SFRs of NGC 7292 they range from $3 \cdot 10^3 M_{\odot}$ to $6 \cdot 10^4 M_{\odot}$. SFRs without emission in the H α line were, on average, less massive in both galaxies, which is likely explained by selection effects.

(4) The measured age of the stellar populations in the SFRs ranges from 2.2 to 18 Myr, with only two regions (both in NGC 7292) being older than 10 Myr. The age of SFRs is clearly correlated with the presence of emission in the H α line: HII regions in galaxies younger than 6-8 Myr ($t = 2.2 - 7.9$ Myr) show H α emission, while older regions ($t = 6.3 - 18$ Myr) do not.

(5) We confirm the conclusion of Gusev et al. (2023b) that EW(H α) and the $R - H\alpha$ index are poor indicators of the age of a young stellar system.

(6) The positions of the SFRs in our sample on the mass-size diagram best match the results from Adamo et al. (2013), extending their dependence for complexes towards smaller star associations. Deviations from the dependence obtained in Adamo et al. (2013) are caused by effects related to the linear resolution of our observations.

ACKNOWLEDGMENTS

The authors thank the reviewer for valuable comments and suggestions. We also express our gratitude to A. E. Perepelitsin (SAO RAS) for technical support with observations using the MaNGaL instrument. This study used open data from the HyperLEDA (<http://leda.univ-lyon1.fr>) and NASA/IPAC Extragalactic Database (<http://ned.ipac.caltech.edu>), Padova group isochrones from the CMD server (<http://stev.oapd.inaf.it>), SExtractor software (<http://sextractor.sourceforge.net>), and the ESO-MIDAS image processing system (<http://www.eso.org/sci/software/esomidas>) developed at the Southern European Observatory.

FUNDING

The development of the instrumentation base of the Caucasian Mountain Observatory of SAI MSU, is supported by the MSU Development Program. The processing and analysis of narrow-band images of NGC 3963 were carried out under the state assignment of the Special Astrophysical Observatory of the Russian Academy of Science, approved by the Ministry of Science and Higher Education of the Russian Federation. VSK thanks the Fund for the Development of Theoretical Physics and Mathematics "BAZIS" (project no. 23-2-2-6-1) for support.

CONFLICT OF INTEREST

The authors of this work declare that they have no conflicts of interest.

References

- Adamo A., Östlin G., Bastian N., Zackrisson E., Livermore R. C., and Guaita L., *Astrophys. J.* 766, 105 (2013).
- Adamo A., Ryon J. E., Messa M., Kim H., et al., *Astrophys. J.* 841, 131 (2017).
- Artamonov B. P., Bruevich V. V., Gusev A. S., Ezhkova O. V., et al., *Astron. Rep.* 54, 1019 (2010).
- Bastian N., Gieles M., Efremov Y. N., and Lamers H. J. G. L. M., *Astron. Astrophys.* 443, 79 (2005).
- Bertelli G., Bressan A., Chiosi C., Fagotto F., and Nasi E., *Astron. Astrophys. Suppl. Ser.* 106, 275 (1994).
- Bolatto A. D., Leroy A. K., Rosolowsky E., Walter F., and Blitz L., *Astrophys. J.* 686, 948 (2008).
- Bressan A., Marigo P., Girardi L., Salasnich B., Dal Cero C., Rubele S., and Nanni A., *Mon. Not. R. Astron. Soc.* 427, 127 (2012).
- Bruevich V. V., Gusev A. S., and Guslyakova S. A., *Astron. Rep.* 54, 375 (2010).
- Calzetti D., Lee J. C., Sabbi E., Adamo A., et al., *Astron. J.* 149, 51 (2015).
- Cerviño M., *New Astron. Rev.* 57, 123 (2013).
- Clem J. L. and Landolt A. U., *Astron. J.* 152, 91 (2016).
- Copetti M. V. F., Pastoriza M. G., and Dottori H. A., *Astron. Astrophys.* 156, 111 (1986).
- de la Fuente Marcos R. and de la Fuente Marcos C., *Astrophys. J.* 700, 436 (2009).
- Efremov Y. N., *Sites of Star Formation in Galaxies: Star Complexes and Spiral Arms* (Nauka, Moscow, 1989) [in Russian].
- Efremov Y. N., *Astron. J.* 110, 2757 (1995).
- Efremov Y. N. and Elmegreen B. G., *Mon. Not. R. Astron. Soc.* 299, 588 (1998).
- Efremov I. N., Ivanov G. R., and Nikolov N. S., *Astrophys. Space Sci.* 135, 119 (1987).
- Elmegreen B. G., *Astrophys. J.* 433, 39 (1994).
- Elmegreen B. G., in *The Galaxy Disk in Cosmological Context, IAU Symposium 254*, Ed. by J. Andersen, B. Nordström, and J. Bland-Hawthorn (2009), p. 289.
- Elmegreen B. G. and Efremov Y. N., *Astrophys. J.* 466, 802 (1996).
- Emsellem E., Schinnerer E., Santoro F., Belfiore F., et al., *Astron. Astrophys.* 659, A191 (2022).
- Gieles M. and Portegies Zwart S. F., *Mon. Not. R. Astron. Soc.* 410, L6 (2011).
- Gouliermis D. A., Elmegreen B. G., Elmegreen D. M., Calzetti D., et al., *Mon. Not. R. Astron. Soc.* 468, 509 (2017).
- Groves B., Kreckel K., Santoro F., Belfiore F., et al., *Mon. Not. R. Astron. Soc.* 520, 4902 (2023).
- Grudić M. Y., Kruijssen J. M. D., Faucher-Giguère C.-A., Hopkins P. F., Ma X., Quataert E., and Boylan-Kolchin M., *Mon. Not. R. Astron. Soc.* 506, 3239 (2021).
- Gusev A. S. and Dodin A. V., *Mon. Not. R. Astron. Soc.* 505, 2009 (2021).

- Gusev A. S. and Shimanovskaya E. V., *Mon. Not. R. Astron. Soc.* 488, 3045 (2019).
- Gusev A. S., Sakhibov F., Piskunov A. E., Kharchenko N. V., et al., *Mon. Not. R. Astron. Soc.* 457, 3334 (2016).
- Gusev A. S., Shimanovskaya E. V., Shatsky N. I., Sakhibov F., Piskunov A. E., and Kharchenko N. V., *Open Astron.* 27, 98 (2018).
- Gusev A. S., Moiseev A. V., and Zheltoukhov S. G., *Astrophys. Bull.* 78, 293 (2023a).
- Gusev A. S., Sakhibov F., Egorov O. V., Kostyuk V. S., and Shimanovskaya E. V., *Mon. Not. R. Astron. Soc.* 525, 742 (2023b).
- Hernández-Martínez L., Peña M., Carigi L., and García-Rojas J., *Astron. Astrophys.* 505, 1027 (2009).
- Hollyhead K., Bastian N., Adamo A., Silva-Villa E., Dale J., Ryon J. E., and Gazak Z., *Mon. Not. R. Astron. Soc.* 449, 1106 (2015).
- Ivanov G. R., *Astrophys. Space Sci.* 178, 227 (1991).
- James P. A., Shane N. S., Beckman J. E., Cardwell A., et al., *Astron. Astrophys.* 414, 23 (2004).
- N. V. Kharchenko N. V., Piskunov A. E., Röser S., Schilbach E., Scholz R.-D., and Zinnecker H., *Astron. Astrophys.* 504, 681 (2009).
- Kim J., Chevance M., Kruijssen J. M. D., Schrubba A., et al., *Mon. Not. R. Astron. Soc.* 504, 487 (2021).
- Kreckel K., Egorov O. V., Belfiore F., Groves B., et al., *Astron. Astrophys.* 667, A16 (2022).
- Landolt A. U., *Astron. J.* 104, 340 (1992).
- Landolt A. U., *Astron. J.* 146, 131 (2013).
- Larson K. L., Lee J. C., Thilker D. A., Whitmore B. C., et al., *Mon. Not. R. Astron. Soc.* 523, 6061 (2023).
- Larson R. B., *Mon. Not. R. Astron. Soc.* 194, 809 (1981).
- Lee J. C., Whitmore B. C., Thilker D. A., Deger S., et al., *Astrophys. J. Suppl.* 258, 10 (2022).
- Moiseev A., Perepelitsyn A., and Oparin D., *Exp. Astron.* 50, 199 (2020).
- Morisset C., Delgado-Inglada G., Sánchez S. F., Galbany L., et al., *Astron. Astrophys.* 594, A37 (2016).
- Odekon M. C., *Astrophys. J.* 681, 1248 (2008).
- Pettini M. and Pagel B. E. J., *Mon. Not. R. Astron. Soc.* 348, L59 (2004).
- Pérez-Montero E., *Mon. Not. R. Astron. Soc.* 441, 2663 (2014).
- Pilyugin L. S. and Grebel E. K., *Mon. Not. R. Astron. Soc.* 457, 3678 (2016).
- Pilyugin L. S. and Mattsson L., *Mon. Not. R. Astron. Soc.* 412, 1145 (2011).
- Piskunov A. E., Kharchenko N. V., Schilbach E., Röser S., Scholz R. D., and Zinnecker H., *Astron. Astrophys.* 525, A122 (2011).
- Portegies Zwart S. F., McMillan S. L. W., and Gieles M., *Ann. Rev. Astron. Astrophys.* 48, 431 (2010).
- Potantin S. A., Belinski A. A., Dodin A. V., Zheltoukhov S. G., et al., *Astron. Lett.* 46, 836 (2020).
- Richer M. G. and McCall M. L., *Astrophys. J.* 445, 642 (1995).
- Rosolowsky E., Hughes A., Leroy A. K., Sun J., et al., *Mon. Not. R. Astron. Soc.* 502, 1218 (2021).
- Scheuermann F., Kreckel K., Barnes A. T., Belfiore F., et al., *Mon. Not. R. Astron. Soc.* 522, 2369 (2023).
- Tang J., Bressan A., Rosenfield P., Slemer A., Marigo P., Girardi L., and Bianchi L., *Mon. Not. R. Astron. Soc.* 445, 4287 (2014).
- Thilker D. A., Whitmore B. C., Lee J. C., Deger S., et al., *Mon. Not. R. Astron. Soc.* 509, 4094 (2022).
- Turner J. A., Dale D. A., Lee J. C., Boquien M., et al., *Mon. Not. R. Astron. Soc.* 502, 1366 (2021).
- van Moorsel G. A., *Astron. Astrophys. Suppl. Ser.* 53, 271 (1983).
- Wei L. H., Keto E., and Ho L. C., *Astrophys. J.* 750, 136 (2012).
- Whitmore B. C., Chandar R., Schweizer F., Rothberg B., et al., *Astron. J.* 140, 75 (2010).
- Whitmore B. C., Chandar R., Kim H., Kaleida C., et al., *Astrophys. J.* 729, 78 (2011).
- Whitmore B. C., Lee J. C., Chandar R., Thilker D. A., et al., *Mon. Not. R. Astron. Soc.* 506, 5294 (2021).

Translated by M. Chubarova

Publisher's Note. Pleiades Publishing remains neutral with regard to jurisdictional claims in published maps and institutional affiliations.